

**Doping-induced disorder and conductivity anisotropy in the spin density wave state of iron pnictides**Dheeraj Kumar Singh<sup>1,2,3,\*</sup> and Yunkyu Bang<sup>2,3,†</sup><sup>1</sup>*School of Physics and Materials Science, Thapar Institute of Engineering and Technology, Patiala 147004, Punjab, India*<sup>2</sup>*Department of Physics, POSTECH, Pohang, Gyeongbuk 790-784, Korea*<sup>3</sup>*Asia Pacific Center for Theoretical Physics, Pohang, Gyeongbuk 790-784, Korea*

(Received 12 January 2020; accepted 10 March 2020; published 1 April 2020)

We examine the role of doped impurity atoms on the conductivity anisotropy of the spin-density wave state in iron pnictides. The conductivity is calculated in a self-consistent spin-density wave state with random impurities in a two-orbital model. We find that the increase in impurity concentration leads to an increased suppression of conductivity in both the antiferromagnetic and ferromagnetic directions. However, the conductivity anisotropy is larger in comparison to the Drude-weight anisotropy in the hole-doped regions. The difference between the two is explained in terms of the anisotropic scattering by the impurities. We demonstrate the effect of the anisotropic impurity scattering by calculating the modulation in the density of states introduced by a single impurity. It is also shown that an increase in the Drude-weight anisotropy with changing carrier concentration, which results mainly from the reconstructed band characteristics, may be directly linked to a similar anisotropy in the density-of-states modulation caused by the impurity atom.

DOI: [10.1103/PhysRevB.101.155101](https://doi.org/10.1103/PhysRevB.101.155101)**I. INTRODUCTION**

Anisotropic electronic properties in iron-based superconductors have been a recurrent theme since the time they were discovered. While anisotropy is naturally expected in the  $(\pi, 0)$  spin-density wave (SDW) state with broken fourfold symmetry, its presence in the paramagnetic nematic as well as in the superconducting state has remained one of the long-standing issues.

The signature of electronic anisotropy in the metallic SDW state is obtained through various experiments such as transport measurement [1–4], optical conductivity [5], angle-resolved photoemission spectroscopy (ARPES) [6,7], and scanning tunneling microscopy (STM) [8–14].

As revealed in the transport measurements, the direction with antiferromagnetic (AFM) spin arrangements is more conducting than the ferromagnetic (FM) direction, a behavior remarkably in contrast with what is expected according to the double-exchange mechanism [15]. The ratio of conductivities in the two directions can be as large as  $\approx 2$ . The anisotropy continues to exist in the doped sample exhibiting the SDW state and also in the nematic phase without any long-range order [16].

Quasiparticle interference (QPI), probed by the STM measurements, can shed light on the nature of impurity scattering and hence on the conductivity anisotropy. Experiments show that the QPI patterns are highly anisotropic and appear nearly one dimensional in the SDW state, nematic phase, and superconducting state. The modulation in the local density of states (LDOS) is stronger along the AFM direction of the SDW state or along the  $a$  axis in the nematic phase with

orthorhombic symmetry. Recent work suggests that the orbital splitting between the  $d_{xz}$  and  $d_{yz}$  orbitals may be crucial in explaining the quasi-one-dimensional nature of QPI patterns.

An insight into the charge dynamics [5] was provided by the theoretical investigation of optical conductivity within the mean-field methods [17–19] as well as by a combined local-density approximation plus dynamical mean-field theory [20]. The in-plane anisotropy was traced to the orbital-weight distribution along the reconstructed Fermi surfaces, which are elliptical in shape [21].

Transport properties in the SDW state have been studied using the memory-function approach [22] and methods based on semiclassical theory [23]. However, the origin of resistivity anisotropy as well as of the doping dependence remains controversial [24,25]. The roles of two important factors are highly debated, namely, the doping-induced (i) disorder and (ii) reconstructed band. An impurity may form elongated magnetic droplets that will enhance the anisotropy [23,26,27] while the interference between scatterings is also expected to play an important role [28]. The features associated with the band structure including the ellipticity of the electron pockets and the Dirac point in the vicinity of the Fermi level were emphasized. The roles of other factors such as critical spin fluctuations have been also investigated [29].

Despite the considerable progress in understanding the anisotropy in electronic properties, it is not clear how the Drude-weight anisotropy and the highly anisotropic QPI patterns are interlinked. Does an anisotropic QPI imply an anisotropy in the Drude weight or conductivity? The answer can provide an important insight into the role of more than one impurity distributed randomly.

In this paper, we address the above questions. In particular, we examine the interplay between the roles of band structure and the doped impurity atoms in the conductivity anisotropy. We consider isotropic impurity scatterers, the presence of

\*dheeraj.kumar@thapar.edu

†ykbang@apctp.org

which in the SDW state is treated self-consistently. Our main finding is that the doping of impurity atoms suppresses the conductivity in both the AFM and FM directions. However, the ratio of the conductivities in the two directions is very sensitive to the way the electrons are scattered as seen in the anisotropy of QPI patterns. The conductivity anisotropy increases in the doped regions where the QPI patterns are highly anisotropic. It is also larger than the Drude-weight anisotropy in the doped regions.

## II. ROLE OF THE BAND STRUCTURE

We consider the model Hamiltonian based on the two  $d$  orbitals  $d_{xz}$  and  $d_{yz}$  [30]. The kinetic-energy part of the Hamiltonian is

$$\mathcal{H}_0 = - \sum_{\langle \mathbf{i}, \mathbf{j} \rangle} \sum_{(\mu, \nu)} \sum_{\sigma} t_{ij}^{\mu\nu} d_{i\mu\sigma}^{\dagger} d_{j\nu\sigma} + \text{H.c.}, \quad (1)$$

where  $d_{i\mu\sigma}^{\dagger}$  ( $d_{i\mu\sigma}$ ) is a creation (destruction) operator for an electron at site  $\mathbf{i}$  in the  $\mu$ th orbital with spin  $\sigma$ . The elements  $t_{ij}^{\mu\nu}$  represent the intra- and interorbital hopping parameters from the  $\mu$ th orbital of site  $\mathbf{i}$  to the  $\nu$ th orbital of site  $\mathbf{j}$ .  $\mu$  and  $\nu$  are the two dominant iron  $3d$  orbitals at the Fermi level namely,  $d_{xz}$  and  $d_{yz}$ . The energy is set in the unit of the intraorbital hopping parameter for the  $d_{xz}$  orbital.

The on-site Coulomb interaction terms responsible for the ordering phenomena in this class of materials are given by

$$\begin{aligned} \mathcal{H}_{\text{int}} = & U \sum_{i, \mu=1,2} n_{i\mu\uparrow} n_{i\mu\downarrow} + \left( U' - \frac{J}{2} \right) \sum_i n_{i1} n_{i2} \\ & - 2J \sum_i \mathbf{S}_{i1} \cdot \mathbf{S}_{i2} + J \sum_{i, \sigma} d_{i1\sigma}^{\dagger} d_{i1\bar{\sigma}}^{\dagger} d_{i2\bar{\sigma}} d_{i2\sigma}. \end{aligned} \quad (2)$$

The first and second terms represent the intra- and interorbital Coulomb interactions, respectively. Here,  $n_{i\mu} = \sum_{\sigma} n_{i\mu\sigma}$  with  $n_{i\mu\sigma} = d_{i\mu\sigma}^{\dagger} d_{i\mu\sigma}$ . The third term describes Hund's coupling where the operator  $S_{i\mu}^p = \sum_{\alpha, \beta} d_{i\mu\alpha}^{\dagger} \sigma_{\alpha\beta}^p d_{i\mu\beta}$  with  $p = x, y, z$ . The fourth term corresponds to the pair-hopping energy. We set  $U' = U - 2J$  and  $J = J'$  for the interaction to be rotation invariant.

For simplicity, we consider the SDW state with tetragonal symmetry. It is worthwhile to note that the SDW state is accompanied with an orthorhombic distortion instead, which, however, is very small:  $\delta = (a - b)/(a + b) \approx 0.003$  [1,31]. Thus, the approach adopted here for the SDW state being considered in the tetragonal symmetry is not a bad approximation when compared with the one with a tiny orthorhombic distortion. The approach is consistent with several earlier works [32]. We consider the following mean-field Hamiltonian in the SDW state originating from the Fermi-surface nesting:

$$\begin{aligned} \mathcal{H}_{\text{SDW}} = & \sum_{\mathbf{k}\sigma} \Psi_{\mathbf{k}\sigma}^{\dagger} \begin{pmatrix} \hat{\varepsilon}_{\mathbf{k}} + \hat{N} & \text{sgn}(\bar{\sigma}) \hat{\Delta} \\ \text{sgn}(\bar{\sigma}) \hat{\Delta} & \hat{\varepsilon}_{\mathbf{k}+\mathbf{Q}} + \hat{N} \end{pmatrix} \Psi_{\mathbf{k}\sigma} \\ = & \sum_{\mathbf{k}\sigma} \Psi_{\mathbf{k}\sigma}^{\dagger} \hat{H}_{\text{MF}} \Psi_{\mathbf{k}\sigma}. \end{aligned} \quad (3)$$

For simplicity, we have considered the magnetization to be along the  $z$  direction.  $\text{sgn}(\bar{\sigma})$  is  $-/+$  for the spins pointing along the positive/negative  $z$  direction. The new electron field

operator is defined as  $\Psi_{\mathbf{k}\sigma}^{\dagger} = (\phi_{\mathbf{k}\sigma}^{\dagger}, \phi_{\mathbf{k}+\mathbf{Q}\sigma}^{\dagger})$  with the ordering wave vector  $\mathbf{Q} = (\pi, 0)$ .  $\phi_{\mathbf{k}\uparrow}^{\dagger} = (d_{\mathbf{k}1\uparrow}^{\dagger}, d_{\mathbf{k}2\uparrow}^{\dagger})$ . The elements of matrices  $\hat{\Delta}$  and  $\hat{N}$  are

$$\begin{aligned} 2\Delta_{11} &= Um_{11} + Jm_{22}, \\ 2\Delta_{22} &= Um_{22} + Jm_{11}, \\ 2\Delta_{12} &= Jm_{12} + (U - 2J)m_{21} \end{aligned} \quad (4)$$

and

$$\begin{aligned} 2N_{11} &= Un_{11} + (2U - 5J)n_{22}, \\ 2N_{22} &= Un_{22} + (2U - 5J)n_{11}, \\ 2N_{12} &= Jn_{12} + (4J - U)n_{21}. \end{aligned} \quad (5)$$

The charge densities and magnetizations are given by

$$n_{\mu\nu} = \sum_{\mathbf{k}\sigma} \langle d_{\mathbf{k}\mu\sigma}^{\dagger} d_{\mathbf{k}\nu\sigma} \rangle, \quad m_{\mu\nu} = \sum_{\mathbf{k}\sigma} \langle d_{\mathbf{k}\mu\sigma}^{\dagger} d_{\mathbf{k}\nu\sigma} \rangle \text{sgn}(\sigma). \quad (6)$$

Here,  $d_{\mathbf{k}\bar{\mu}\sigma}^{\dagger} = d_{\mathbf{k}+\mathbf{Q}\mu\sigma}^{\dagger}$  with the bar over orbital indices indicating the momentum shift of  $\mathbf{Q} = (\pi, 0)$ . The momentum summation over  $\mathbf{k}$  is carried out in the reduced Brillouin zone.

We first examine the Drude-weight anisotropy in the SDW state, which can reveal the role of Fermi-surface reconstruction and the orbital-weight redistribution in the conductivity anisotropy. The Drude weight can be obtained as the  $\omega \rightarrow 0$  limit of the optical conductivity, i.e. [33,34],

$$\begin{aligned} \frac{D_{\alpha}}{2\pi} = & \frac{1}{2N} \sum_{\mathbf{k}} T_{ll}^{\alpha}(\mathbf{k}) \theta(-\varepsilon_{l\mathbf{k}}) - \frac{1}{N} \sum_{\mathbf{k}, l \neq l'} \frac{|J_{ll'}^{\alpha}(\mathbf{k})|^2}{\varepsilon_{l'\mathbf{k}} - \varepsilon_{l\mathbf{k}}} \\ & \times \theta(-\varepsilon_{l'\mathbf{k}}) \theta(\varepsilon_{l\mathbf{k}}). \end{aligned} \quad (7)$$

$\theta$  is the step function,  $\varepsilon_{l\mathbf{k}}$  is the single-particle energy in the SDW state, and the integer  $l$  denotes the band number. We also note

$$\begin{aligned} T_{ll}^{\alpha} = & \sum_{\mu\nu} T_{ll}^{\alpha; \mu\nu} = \sum_{\mu\nu} \frac{\partial^2 t^{\mu\nu}(\mathbf{k})}{\partial k_x^2} c_{\mathbf{k}\mu l}^* c_{\mathbf{k}\nu l}, \\ J_{ll'}^{\alpha} = & - \sum_{\mu\nu} J_{ll'}^{\alpha; \mu\nu} = - \sum_{\mu\nu} \frac{\partial t^{\mu\nu}(\mathbf{k})}{\partial k_x} c_{\mathbf{k}\mu l}^* c_{\mathbf{k}\nu l}. \end{aligned} \quad (8)$$

$c_{\mathbf{k}\mu l}$  is the unitary matrix element between the orbital  $\mu$  and band  $l$  in the ordered state.

Figure 1(a) shows the orbital contributions to the overall density of states (DOS) at the Fermi level. The contributions from the  $d_{xz}$  and  $d_{yz}$  orbitals are nearly the same in the electron-doped region but differ significantly within a large window of the hole-doped region. This indicates that the maximum in the anisotropy may shift into the hole-doped region. The asymmetry about zero doping can arise as the sizes of the hole and electron pockets change differently on doping holes and electrons. Similar anisotropy for conductivity in the hole- and electron-doped region was noted in the paramagnetic phase using spin fluctuations [29]. It is to be noted that the chemical potential for zero doping in the two-orbital model corresponds to the half filling  $n = 2$ , which is different for the models involving more than two orbitals. But a closer look at the reconstructed Fermi surface in the SDW state (Fig. 2) for different band filling shows that the band filling

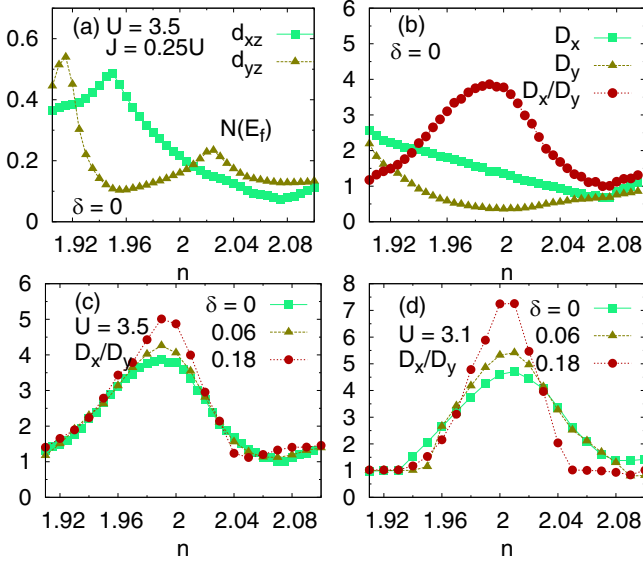


FIG. 1. (a) The orbital-resolved density of states in the self-consistently obtained SDW state at the Fermi level. The intra-orbital Coulomb interaction  $U = 3.5$  and Hund's coupling  $J = 0.25U$ . (b) The Drude weights  $D_x$  along the  $x$  (antiferromagnetic) direction,  $D_y$  along the  $y$  (ferromagnetic) direction, and their ratio  $D_x/D_y$  as a function of doping. (c, d) Drude-weight anisotropy for various orbital-splitting strengths  $-\delta \sum_i (d_{ixz}^\dagger d_{ixz} - d_{iyz}^\dagger d_{iyz})$  explicitly included in the Hamiltonian for two different intraorbital interactions.

$n \approx 1.9$  appears to reproduce the experimental Fermi surface better for the undoped SDW state. As also observed in the ARPES measurements, the pockets closer especially to the high-symmetry point  $\Gamma$  can be easily noticed.

Figure 1(b) shows the Drude weights  $D_x$  and  $D_y$  along the AFM and FM directions, respectively, calculated as a function of doping. Both  $D_x$  and  $D_y$  get reduced on moving from the hole-doped region towards the electron-doped region. Interestingly, the ratio  $D_x/D_y$  exhibits a maximum in the hole-doped region near  $n \approx 2$ , a behavior remarkably similar to the more sophisticated three- and five-orbital model [35]. The ratio decreases on either side of  $n \approx 2$ , thus being inconsistent with the experiments on the electron-doped side.

From the structure of Eqs. (7) and (8), the individual contributions due to the intra- and interorbital hopping can also be analyzed. We have checked that as one moves from the hole- to the electron-doped region the contribution due to the intraorbital hopping of the  $d_{xz}$  orbital, which is larger along the ferromagnetic direction, decreases so that on reaching the electron-doped region its contribution becomes larger along the antiferromagnetic direction. This can be understood from the orbital content along the Fermi surface and Fermi velocity. For electron doping and the  $d_{xz}$  orbital dominated regions of Fermi surfaces, Fermi velocity along  $k_x$  is larger than along  $k_y$  over a significant portion [Figs. 2(a)–2(f)]. Exactly the opposite behavior is exhibited by the  $d_{yz}$  orbital as expected. On the other hand, the interorbital hopping contribution continues to decrease from the hole- to the electron-doped region.

We also examined the consequence of an explicit orbital splitting term  $-\delta \sum_i (d_{ixz}^\dagger d_{ixz} - d_{iyz}^\dagger d_{iyz})$  introduced in the

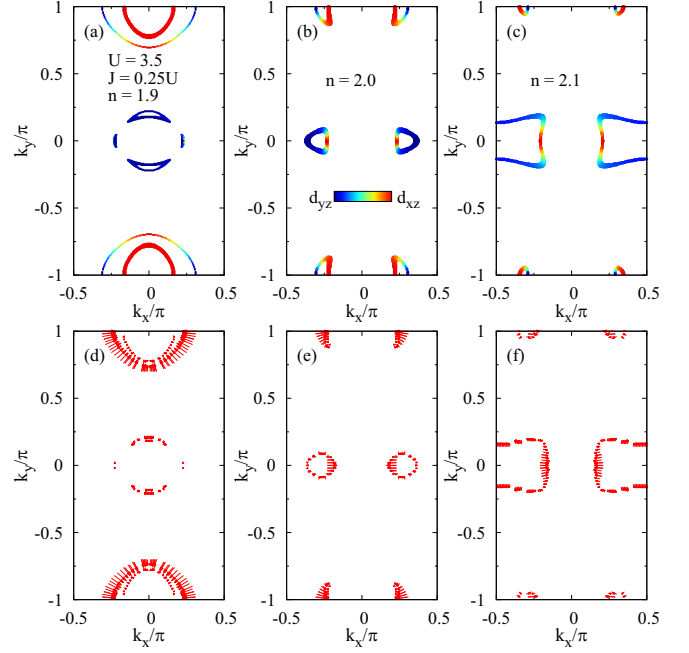


FIG. 2. The Fermi surfaces in the  $(\pi, 0)$  SDW state for (a) hole doping  $x_h = 0.1$ , (b)  $x_h = 0.0$ , and electron doping (c)  $x_e = 0.1$  with the predominant orbital densities, where  $U = 3.5$  and  $J = 0.25U$ . The reference for doping is the band filling  $n = 2.0$  which is assumed to correspond to zero doping. The Fermi velocities along the Fermi surfaces for (a)–(c) are shown in (d)–(f), respectively. The length of the arrows in (d)–(f) is proportional to the magnitude of the Fermi velocity.

original Hamiltonian [Eqs. (1) and (2)]. Note that the order parameters are calculated self-consistently for the SDW state in the presence of the orbital-splitting term. Drude weight for different  $\delta$  is shown in Figs. 1(c) and 1(d) for two interactions  $U = 3.5$  and  $3.1$ , respectively. A larger  $U$  corresponds to a larger value of magnetic moment and a significant Fermi-surface reconstruction. Therefore the effect of  $\delta$  in the conductivity anisotropy is suppressed. On the other hand, for a smaller  $U$  and therefore for a smaller magnetic moment,  $\delta$  introduces a significant anisotropy as can be noticed from Fig. 1(d).

### III. SINGLE IMPURITY SCATTERING AND DENSITY-OF-STATES MODULATION

In the following, we examine the role of a single impurity in introducing change in the electronic state. This can prove to be very useful in understanding the nature of scatterings. Especially, the possible link between the conductivity anisotropy and the anisotropic impurity scattering may be unraveled. To achieve this objective, the impurity effect is treated within the  $t$ -matrix approximation. The change in the DOS because of a nonmagnetic impurity atom can be obtained as in Ref. [32].

The change in the DOS is given by

$$\delta\rho(\mathbf{q}, \omega) = \sum_{\alpha} \delta\rho_{\alpha}(\mathbf{q}, \omega) = \frac{i}{2\pi} \sum_{\mathbf{k}\alpha} g_{\alpha}(\mathbf{k}, \mathbf{q}, \omega) \quad (9)$$

with

$$\begin{aligned}
 g_0(\mathbf{k}, \mathbf{q}, \omega) &= \text{Tr} \delta \hat{G}(\mathbf{k}, \mathbf{k}', \omega) - \text{Tr} \delta \hat{G}^*(\mathbf{k}', \mathbf{k}, \omega), \\
 g_1(\mathbf{k}, \mathbf{q}, \omega) &= \sum_{\mu \leq 2} [\delta G_{\mu, \mu+2}(\mathbf{k}, \mathbf{k}', \omega) - \delta G_{\mu, \mu+2}^*(\mathbf{k}', \mathbf{k}, \omega)], \\
 g_2(\mathbf{k}, \mathbf{q}, \omega) &= \sum_{\mu \leq 2} [\delta G_{\mu+2, \mu}(\mathbf{k}, \mathbf{k}', \omega) - \delta G_{\mu+2, \mu}^*(\mathbf{k}', \mathbf{k}, \omega)]
 \end{aligned} \tag{10}$$

and corresponding LDOS modulation can be obtained as

$$\begin{aligned}
 \delta \rho(\mathbf{r}_i, \omega) &= \frac{1}{N} \sum_{\mathbf{q}} \left[ \delta \rho_0(\mathbf{q}, \omega) e^{i\mathbf{q} \cdot \mathbf{r}_i} + \delta \rho_1(\mathbf{q}, \omega) e^{i(\mathbf{q}-\mathbf{Q}) \cdot \mathbf{r}_i} \right. \\
 &\quad \left. + \delta \rho_2(\mathbf{q}, \omega) e^{i(\mathbf{q}+\mathbf{Q}) \cdot \mathbf{r}_i} \right].
 \end{aligned} \tag{11}$$

Here,  $\mathbf{q} = \mathbf{k} - \mathbf{k}'$ . The superscript \* denotes the complex conjugate. The change in the Green's-function matrix due to a single nonmagnetic impurity is

$$\delta \hat{G}(\mathbf{k}, \mathbf{k}', \omega) = \hat{G}^0(\mathbf{k}, \omega) \hat{\mathcal{T}}(\omega) \hat{G}^0(\mathbf{k}', \omega), \tag{12}$$

where the mean-field Green's function is given by

$$\hat{G}^0(\mathbf{k}, \omega) = [(\omega + i\eta)\hat{\mathbf{1}} - \hat{H}_{\text{MF}}(\mathbf{k})]^{-1}. \tag{13}$$

The mean-field Hamiltonian  $\hat{H}_{\text{MF}}(\mathbf{k})$  is defined in the orbital basis [Eq. (3)]. The  $t$  matrix is obtained as

$$\hat{\mathcal{T}}(\omega) = [\hat{\mathbf{1}} - \hat{V} \hat{G}(\omega)]^{-1} \hat{V}. \tag{14}$$

$\hat{\mathbf{1}}$  is a  $4 \times 4$  identity matrix.

The momentum averaged Green's function is defined as

$$\hat{G}(\omega) = \frac{1}{N} \sum_{\mathbf{k}} \hat{G}^0(\mathbf{k}, \omega) \tag{15}$$

while the impurity matrix

$$\hat{V} = V_{\text{imp}} \begin{pmatrix} \hat{\mathbf{1}} & \hat{\mathbf{1}} \\ \hat{\mathbf{1}} & \hat{\mathbf{1}} \end{pmatrix}. \tag{16}$$

$\hat{\mathbf{1}}$  is the  $2 \times 2$  identity matrix.

Figures 3(a)–3(c) show the contours of constant energy (CCEs) for the quasiparticle excitation energy  $\omega = 0$  for various band fillings  $n = 1.95, 2.00, 2.05$ , where  $U = 3.2$  and  $J = 0.25U$ . The nature of the QPI patterns can be understood with the help of vectors which connect different portions of the CCEs. The spectral density varies along the CCEs, thus the scattering vectors connecting the regions with a large spectral density will dominate the scattering process. Since we are considering only the intraorbital scattering processes, the scattering vectors connecting the portions dominated by the same orbital will lead to the dominant patterns in the QPI.

QPIs are shown in Figs. 3(d)–3(f). The QPI pattern is elliptical in shape for  $n = 1.9$ , which results from the large electron pocket around  $(\pi, 0)$ . This is in a good qualitative agreement with the experiments. As the electron concentration increases, the electron pocket around  $(\pi, 0)$  splits in two parts. These parts move away from each other [Fig. 3(b)]. The split pockets together with the pockets around  $\Gamma$  lead to the

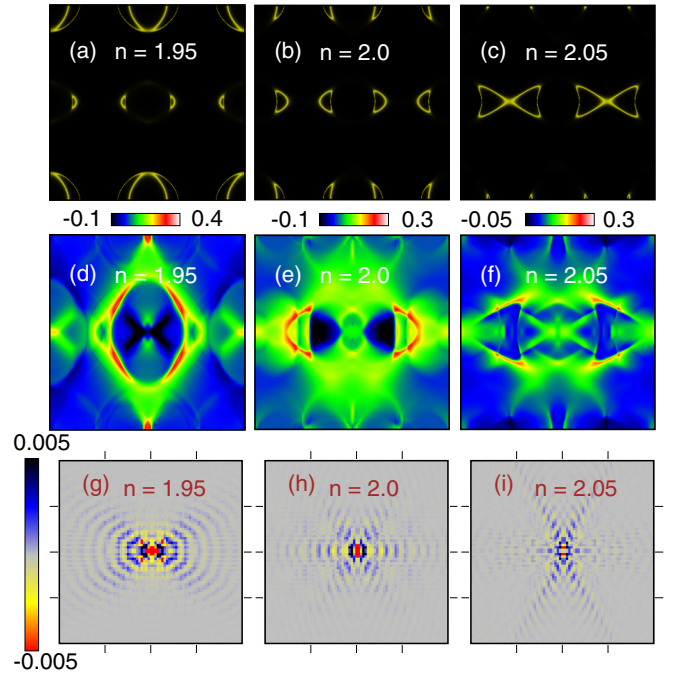


FIG. 3. (a), (b), and (c) show the constant energy surfaces for band fillings  $n = 1.95, 2.00$ , and  $2.05$ , respectively for  $\omega = 0$ . (d)–(f) and (g)–(i) show the corresponding density-of-states modulation in the momentum and real space, respectively. The units of momentum space plots are in  $\pi/a$  with range  $[-1, 1]$ . The real-space plots are in the units of  $a$  with range  $[-40, 40]$ . Local density-of-states modulation is shown for  $80 \times 80$  lattice size, with the impurity atom located at the center. Note that the actual calculation has been done for  $300 \times 300$  lattice size.

QPI pattern in Fig. 3(e). It can be noted that the pattern is dominated by the growing pockets around  $\Gamma$  in the electron-doped region.

Figures 3(g)–3(i) show the density-of-states modulation in the vicinity of impurity atoms. The calculation is carried out for  $300 \times 300$ , but the results are shown for  $80 \times 80$  with the impurity atom at the center for the sake of better visibility. When  $n = 1.9$ , we find that the modulation is stronger along  $x$  (the AFM direction) with wavelength  $8a_{\text{Fe-Fe}}$  in comparison to  $y$ .  $a_{\text{Fe-Fe}}$  is the distance between nearest-neighbor iron atoms. Interestingly, though the modulation wavelength along  $x$  agrees well with the STM measurements for the electron-doped  $\text{Ca}(\text{Fe}_{1-x}\text{Co}_x)_2\text{As}_2$ , the strongest modulation occurs along angle  $\pi/4$  with positive  $x$ . On the other hand, for  $n = 2.0$ , the strongest modulation occurs along  $x$ . Finally, there is no clear modulation along either  $x$  or  $y$  in the electron-doped region  $n \approx 2.05$ .

Although the single impurity treatment does provide a useful insight into understanding the scattering mechanism and especially the role of the band structure, the doped compound contains more than one impurity. Therefore, the interference between the scattering events from multiple impurities may present a different picture altogether. In the next section, we numerically diagonalize the finite system with multiple impurities to capture any interference effect between the impurities beyond the one impurity problem.

#### IV. MORE THAN ONE IMPURITY ATOM AND CONDUCTIVITY ANISOTROPY

In the following, we examine the conductivity anisotropy of the SDW state in the presence of multiple impurities. The effect of the doped impurity atom potential is incorporated as

$$\mathcal{H}_{\text{imp}} = V_{\text{imp}} \sum_{\mathbf{i}, \mu, \sigma} \delta_{\mathbf{i}\mathbf{i}'} d_{\mathbf{i}\mu\sigma}^\dagger d_{\mathbf{i}\mu\sigma} \quad (17)$$

in the Hamiltonian, where  $\mathbf{i}'$  corresponds to the lattice sites which are chemically substituted.  $V_{\text{imp}}$  is the impurity potential or scattering strength, which is taken to be of the order of the largest interaction  $U$  in the system. The number of impurity atoms is chosen to correspond to the band filling with  $n = 2$  as a reference for zero doping. For instance,  $n = 2.05$  corresponds to the 5% impurity atoms. Since the doped sites occur randomly while preparing the samples in the experiments, in accordance with it, the doping sites are selected at random in the calculation as well.

The mean-field decoupling of the interaction part yields the real-space Hamiltonian in the presence of randomly located impurity atoms:

$$\mathcal{H}_{\mathbf{ij}\sigma}^{\mu\nu} = t_{\mathbf{ij}\sigma}^{\mu\nu} + \delta_{\mathbf{i}\mathbf{i}'} \delta_{\mu\nu} \left[ \delta_{\mathbf{i}\mathbf{i}'} V_{\text{imp}} + \frac{5J - U}{2} n_{i\mu} + \frac{1}{2} \text{sgn}(\bar{\sigma}) \left( U m_{i\mu} + \sum_{\mu' \neq \nu'} J m_{i\nu'} \right) \right]. \quad (18)$$

Here, the charge density is  $n_{i\mu} = \sum_{l\sigma} |u_{i\mu\sigma}^l|^2 f(\varepsilon_{l\sigma})$  with  $u_{i\mu\sigma}^l$  being the element of the unitary matrix diagonalizing the Hamiltonian matrix for  $N_x \times N_y$  lattice sites. Magnetization  $m_{i\mu} = n_{i\mu\uparrow} - n_{i\mu\downarrow}$  for each of the orbitals is determined self-consistently by diagonalizing the Hamiltonian. The inter-orbital terms involving  $n_{i\mu\nu}$  and  $m_{i\mu\nu}$  are neglected for simplicity as their contribution is negligibly small.  $\text{sgn}(\sigma)$  is  $+/-$  for the spins pointing along the positive/negative  $z$  direction.

Conductivity is calculated using the Kubo-Greenwood formula

$$K = \frac{K_o}{N} \sum_{\alpha\beta} \frac{f_\alpha - f_\beta}{\varepsilon_\beta - \varepsilon_\alpha} |\langle \alpha | \hat{j}_x | \beta \rangle|^2 \delta[\omega - (\varepsilon_\beta - \varepsilon_\alpha)], \quad (19)$$

where  $K_o = \pi e^2/h$ ,  $f$  is the Fermi function, and  $\varepsilon_\alpha$  is the energy corresponding to eigenstate  $|\alpha\rangle$ . The charge-current operators along  $x$  and  $y$  are

$$\begin{aligned} \hat{j}_x &= \sum_{\mathbf{i}, \mathbf{r}=\mathbf{x}, \mathbf{x}+\mathbf{y}, \mathbf{x}-\mathbf{y}} \sum_{\mu, \nu, \sigma} -it_{\mathbf{i}, \mathbf{i}+\mathbf{r}}^{\mu\nu} (d_{\mathbf{i}\mu\sigma}^\dagger d_{\mathbf{i}+\mathbf{r}\nu\sigma} - \text{H.c.}), \\ \hat{j}_y &= \sum_{\mathbf{i}, \mathbf{r}=\mathbf{y}, \mathbf{y}+\mathbf{x}, \mathbf{y}-\mathbf{x}} \sum_{\mu, \nu, \sigma} -it_{\mathbf{i}, \mathbf{i}+\mathbf{r}}^{\mu\nu} (d_{\mathbf{i}\mu\sigma}^\dagger d_{\mathbf{i}+\mathbf{r}\nu\sigma} - \text{H.c.}), \end{aligned} \quad (20)$$

respectively.  $t_{\mathbf{i}\mathbf{i}'}^{\mu\nu}$  is the hopping from the orbital  $\mu$  at site  $\mathbf{i}$  to the orbital  $\nu$  at site  $\mathbf{i} + \mathbf{r}$ .  $\mathbf{i} + \mathbf{r}$  includes the nearest and next-nearest neighbors (with positive  $\mathbf{x}$ ).  $\mathbf{x}$  and  $\mathbf{y}$  are the unit lattice vectors connecting the nearest neighbors along  $x$  and  $y$  directions, respectively.

For the system size  $16 \times 16$ , the associated mean energy-level spacing  $s$  is roughly 0.01. Therefore, it is difficult to obtain a meaningful result for the conductivity when it is calculated for such a small-sized but moderately correlated

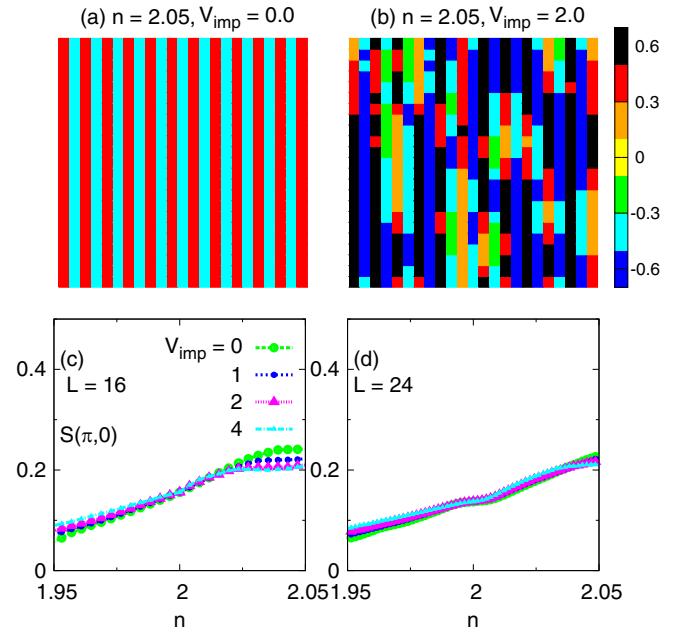


FIG. 4. Magnetic moments in the self-consistent SDW state with the (a) absence and (b) presence of 5% random impurities ( $V_{\text{imp}} = 0$  corresponds to no impurity scattering or to simply the absence of impurities). The structure factor  $S(\mathbf{Q})$  is shown for the lattice sizes (c)  $16 \times 16$  and (d)  $24 \times 24$ .

system with significant presence of DOS at the Fermi level as revealed in the ARPES measurements. To circumvent this problem, we consider the superlattice or replica method, where a self-consistently obtained state on a lattice of size  $16 \times 16$  is replicated eight times in both the  $x$  and  $y$  directions. This can be achieved by using the Bloch theorem, which yields the twisted or complex boundary conditions. Then,  $8 \times 8 = 64$  matrices of the size  $512 \times 512$  need to be diagonalized to obtain eigenenergies for each self-consistent state. This step leads to a significant increase in the number of energy levels in the vicinity of the Fermi level as the mean level spacing  $s$  is reduced to  $\approx 0.00015$ .

The procedure for obtaining the conductivity involves the following processes. The delta-function broadening  $\delta$  in the conductivity calculation for the  $128 \times 128$  system is chosen to be  $W/(128^2) \approx 0.0008$ , where the bandwidth  $W = 12$ . Instead of calculating conductivity at  $\omega = 0$ , we choose a very small frequency  $\omega = 0.00001 \approx 0.1s$ . Then, conductivities are calculated for ten frequencies in the range  $[0.1s, 0.1s + \delta]$  with increments of  $0.1\delta$ , and thereafter an average of these conductivities is obtained, which is taken as the dc conductivity. The conductivity thus obtained is further averaged over ten different randomly distributed impurity configurations.

Figures 4(a) and 4(b) show the magnetic order both in the presence and absence of impurities, respectively. The collinear magnetic order is modulated significantly in the vicinity of impurity atoms. But this has only a weak effect on the structure factor calculated as  $S(\mathbf{Q}) = \sum_{\mathbf{i}\mathbf{j}} m_{\mathbf{i}} m_{\mathbf{j}} e^{i\mathbf{Q} \cdot (\mathbf{R}_{\mathbf{i}} - \mathbf{R}_{\mathbf{j}})}$ . We have also investigated the lattice size dependence of the structure factor; it shows a weak dependence especially near the size  $18 \times 18$  considered in this paper.

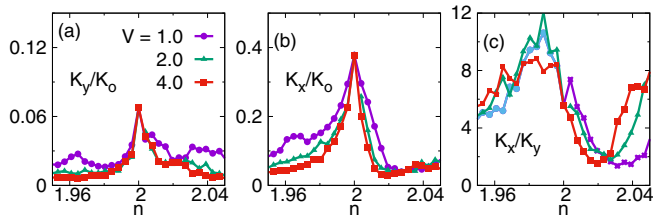


FIG. 5. The conductivity along the ferromagnetic (a) and anti-ferromagnetic (b) directions as a function of doping, where  $K_0 = \pi e^2/h$ . (c) The ratio of conductivities along the antiferromagnetic and ferromagnetic directions.

Figure 5 shows the results obtained for the conductivity using the above procedure. The conductivities in both the FM [Fig. 5(a)] and the AFM [Fig. 5(b)] directions are quickly suppressed as the number of impurity atoms increases on either side of zero doping. This is in contrast with the monotonic Drude-weight behavior along the two directions in the vicinity of zero doping. For instance,  $D_x$  continues to decrease from the hole- to the electron-doped region. The suppression shows only a slight increase with the impurity scattering strength in the small window of  $V_{\text{imp}} = 1\text{--}4$  eV.

Figure 5(c) shows the ratio of conductivities  $K_x/K_y$  along the AFM and FM directions. It can be noticed that  $K_x/K_y \approx D_x/D_y$  for zero doping as expected. Although the shape of  $K_x/K_y$  is almost the same as that of  $D_x/D_y$ ,  $K_x/K_y > D_x/D_y$  in the hole-doped region. Thus, the scattering due to the impurity atoms results in an enhancement of conductivity anisotropy of the SDW state. Moreover, we also find that the ratio increases on electron doping for larger  $V_{\text{imp}}$ .

## V. DISCUSSION

The Drude-weight anisotropy gives an important insight into the anisotropic electronic band structure including the orbital contents as well as the geometry of the Fermi surface. The details of QPI structure are also highly dependent on the reconstructed bands in the SDW state. Therefore, a direct link between the anisotropic scattering due to a single impurity with isotropic scattering strength and the Drude-weight anisotropy is naturally expected. As can be noticed that  $D_x/D_y$  is peaked near  $n \approx 1.98$ , where the QPI also shows a strongest modulation along the AFM direction. In contrast,  $D_x/D_y \approx 1.0$  for  $n \approx 2.05$ , which is consistent with the modulation in the QPI being strong neither along the AFM nor along the FM direction [21].

Several aspects of the electronic anisotropy explored in the two-orbital model can be noticed also in the five-orbital models [36]. For instance, the behavior of the Drude-weight anisotropy in the vicinity of  $n = 2$  for zero doping in the two-orbital model is similar to that in the five-orbital model for  $n = 6$  (zero doping) [35]. First, the peak in the anisotropy occurs in the vicinity of zero doping. Secondly, the anisotropy decreases on both electron and hole doping. The only difference is that the degree of anisotropy is slightly larger in the two-orbital model. Therefore, the QPI modulation along the AFM direction is expected to be stronger in

comparison with the five-orbital model, which is indeed the case [37].

The presence of orbital splitting between  $d_{xz}$  and  $d_{yz}$  orbitals for various pnictides and chalcogenides has been observed in the high-temperature nematic phase as well as in the low-temperature superconducting state. Therefore, the splitting should be also present in the the SDW state. But the origin of the splitting is different from the one introduced because of the breaking of fourfold symmetry by the SDW transition. It is worthwhile to note that the one-dimensional characteristic of the QPI patterns has been attributed to the orbital splitting and it will further enhance the Drude-weight anisotropy.

We find that the nature of conductivity anisotropy in the presence of multiple impurities is in qualitative agreement with the behavior of Drude weight and QPI. The higher Drude-weight anisotropy corresponds to a highly anisotropic QPI pattern, and both, in turn, indicate a highly anisotropic conductivity as demonstrated through the current paper. Although our paper is based on the two-orbital model, a similar behavior of the QPI and Drude-weight anisotropy is obtained within a more realistic five-orbital model. The calculation of conductivity anisotropy based on a self-consistent treatment of more than one impurity is a daunting task within a five-orbital model. We believe the results obtained here within the two-orbital model will be qualitatively similar to those expected in a more sophisticated model. Therefore, our paper also brings out the limitation of the tight-binding models in capturing the behavior of the conductivity anisotropy for electron doping.

## VI. CONCLUSIONS

In conclusion, we have examined the conductivity in a self-consistently obtained spin-density wave state of iron pnictides when multiple random impurities are present. The conductivity anisotropy shows a behavior similar to the Drude-weight anisotropy. However, in order to explain the experimentally observed conductivity anisotropy quantitatively, it is crucial to take the effect of the anisotropic scattering by isotropic impurity into account in a fully self-consistent manner. This was demonstrated through the quasiparticle interference in this paper. We find that the increase in the anisotropy on electron doping cannot be captured even though the random impurities are treated self-consistently. We argued that a similar result is also expected in the five-orbital models. Thus, our paper points out the limitation of tight-binding models in the electron-doped SDW state.

## ACKNOWLEDGMENTS

We acknowledge the use of high-performance computing clusters at HRI. D.K.S. would like to thank P. Majumdar, I. Eremin, and A. Akbari for critical comments and suggestions. D.K.S. and Y.B. were supported through NRF Grants No. 2016-R1A2B4-008758 and No. 2019-R1H1A2-079920 funded by the National Research Foundation of Korea.

- [1] J.-H. Chu, J. G. Analytis, K. De Greve, P. L. McMahon, Z. Islam, Y. Yamamoto, and I. R. Fisher, *Science* **329**, 824 (2010).
- [2] M. A. Tanatar, E. C. Blomberg, A. Kreyssig, M. G. Kim, N. Ni, A. Thaler, S. L. Bud'ko, P. C. Canfield, A. I. Goldman, I. I. Mazin, and R. Prozorov, *Phys. Rev. B* **81**, 184508 (2010).
- [3] I. R. Fisher, L. Degiorgi, and Z. X. Shen, *Rep. Prog. Phys.* **74**, 124506 (2011).
- [4] J. J. Ying, X. F. Wang, T. Wu, Z. J. Xiang, R. H. Liu, Y. J. Yan, A. F. Wang, M. Zhang, G. J. Ye, P. Cheng, J. P. Hu, and X. H. Chen, *Phys. Rev. Lett.* **107**, 067001 (2011).
- [5] M. Nakajima, T. Liang, S. Ishida, Y. Tomioka, K. Kihou, C. H. Lee, A. Iyo, H. Eisaki, T. Kakeshita, T. Ito, and S. Uchida, *Proc. Natl. Acad. Sci. USA* **108**, 12238 (2011).
- [6] M. Yi, D. Lu, J.-H. Chu, J. G. Analytis, A. P. Sorini, A. F. Kemper, B. Moritz, S.-K. Mo, R. G. Moore, M. Hashimoto, W.-S. Lee, Z. Hussain, T. P. Devereaux, I. R. Fisher, and Z.-X. Shen, *Proc. Natl. Acad. Sci. USA* **108**, 6878 (2011).
- [7] T. Shimojima, T. Sonobe, W. Malaeb, K. Shinada, A. Chainani, S. Shin, T. Yoshida, S. Ideta, A. Fujimori, H. Kumigashira, K. Ono, Y. Nakashima, H. Anzai, M. Arita, A. Ino, H. Namatame, M. Taniguchi, M. Nakajima, S. Uchida, Y. Tomioka, T. Ito, K. Kihou, C. H. Lee, A. Iyo, H. Eisaki, K. Ohgushi, S. Kasahara, T. Terashima, H. Ikeda, T. Shibauchi, Y. Matsuda, and K. Ishizaka, *Phys. Rev. B* **89**, 045101 (2014).
- [8] T.-M. Chuang, M. P. Allan, J. Lee, Y. Xie, N. Ni, S. L. Bud'ko, G. S. Boebinger, P. C. Canfield, and J. C. Davis, *Science* **327**, 181 (2010).
- [9] M. P. Allan, T.-M. Chuang, F. Massee, Y. Xie, N. Ni, S. L. Bud'ko, G. S. Boebinger, Q. Wang, D. S. Dessau, P. C. Canfield, M. S. Golden, and J. C. Davis, *Nat. Phys.* **9**, 220 (2013).
- [10] E. P. Rosenthal, E. F. Andrade, C. J. Arguello, R. M. Fernandes, L. Y. Xing, X. C. Wang, C. Q. Jin, A. J. Millis, and A. N. Pasupathy, *Nat. Phys.* **10**, 225 (2014).
- [11] D. Huang, T. A. Webb, S. Fang, C.-L. Song, C.-Z. Chang, J. S. Moodera, E. Kaxiras, and J. E. Hoffman, *Phys. Rev. B* **93**, 125129 (2016).
- [12] U. R. Singh, S. C. White, S. Schmaus, V. Tsurkan, A. Loidl, J. Deisenhofer, and P. Wahl, *Sci. Adv.* **1**, e1500206 (2015).
- [13] A. Kostin, P. O. Sprau, A. Kreisel, Y. X. Chong, A. E. Böhmer, P. C. Canfield, P. J. Hirschfeld, B. M. Andersen, and J. C. S. Davis, *Nat. Mater.* **17**, 869 (2018).
- [14] T. Hanaguri, K. Iwaya, Y. Kohsaka, T. Machida, T. Watashige, S. Kasahara, T. Shibauchi, and Y. Matsuda, *Sci. Adv.* **4**, eaar6419 (2018).
- [15] C. Zener, *Phys. Rev.* **82**, 403 (1951).
- [16] E. C. Blomberg, M. A. Tanatar, R. M. Fernandes, I. I. Mazin, B. Shen, H.-H. Wen, M. D. Johannes, J. Schmalian, and R. Prozorov, *Nat. Commun.* **4**, 1914 (2013).
- [17] B. Valenzuela, E. Bascones, and M. J. Calderón, *Phys. Rev. Lett.* **105**, 207202 (2010).
- [18] K. Sugimoto, E. Kaneshita, and T. Tohyama, *J. Phys. Soc. Jpn.* **80**, 033706 (2011).
- [19] X. Zhang and E. Dagotto, *Phys. Rev. B* **84**, 132505 (2011).
- [20] Z. P. Yin, K. Haule, and G. Kotliar, *Nat. Phys.* **7**, 294 (2011).
- [21] D. K. Singh and P. Majumdar, *Phys. Rev. B* **98**, 195130 (2018).
- [22] K. Sugimoto, P. Prelovšek, E. Kaneshita, and T. Tohyama, *Phys. Rev. B* **90**, 125157 (2014).
- [23] M. N. Gastiasoro, I. Paul, Y. Wang, P. J. Hirschfeld, and B. M. Andersen, *Phys. Rev. Lett.* **113**, 127001 (2014).
- [24] H.-H. Kuo and I. R. Fisher, *Phys. Rev. Lett.* **112**, 227001 (2014).
- [25] T. Kobayashi, K. Tanaka, S. Miyasaka, and S. Tajima, *J. Phys. Soc. Jpn.* **84**, 094707 (2015).
- [26] M. Breitzkreuz, P. M. R. Brydon, and C. Timm, *Phys. Rev. B* **90**, 121104(R) (2014).
- [27] Y. Wang, Maria N. Gastiasoro, Brian M. Andersen, M. Tomic, H. O. Jeschke, R. Valenti, I. Paul, and P. J. Hirschfeld, *Phys. Rev. Lett.* **114**, 097003 (2015).
- [28] R. M. Fernandes, E. Abrahams, and J. Schmalian, *Phys. Rev. Lett.* **107**, 217002 (2011).
- [29] A. F. Kemper, M. M. Korshunov, T. P. Devereaux, J. N. Fry, H.-P. Cheng, and P. J. Hirschfeld, *Phys. Rev. B* **83**, 184516 (2011).
- [30] S. Raghu, X.-L. Qi, C.-X. Liu, D. J. Scalapino, and S.-C. Zhang, *Phys. Rev. B* **77**, 220503(R) (2008).
- [31] S. Kasahara, H. J. Shi, K. Hashimoto, S. Tonegawa, Y. Mizukami, T. Shibauchi, K. Sugimoto, T. Fukuda, T. Terashima, A. H. Nevidomskyy, and Y. Matsuda, *Nature (London)* **486**, 382 (2012).
- [32] J. Knolle, I. Eremin, A. Akbari, and R. Moessner, *Phys. Rev. Lett.* **104**, 257001 (2010); A. Akbari, J. Knolle, I. Eremin, and R. Moessner, *Phys. Rev. B* **82**, 224506 (2010); I. I. Mazin, S. A. J. Kimber, and D. N. Argyriou, *ibid.* **83**, 052501 (2011); N. Plonka, A. F. Kemper, S. Graser, A. P. Kampf, and T. P. Devereaux, *ibid.* **88**, 174518 (2013); H.-Y. Zhang and J.-X. Li, *ibid.* **94**, 075153 (2016); D. K. Singh, *J. Phys. Chem. Solids* **112**, 246 (2018).
- [33] E. Dagotto, *Rev. Mod. Phys.* **66**, 763 (1994).
- [34] B. Valenzuela, M. J. Calderón, G. León, and E. Bascones, *Phys. Rev. B* **87**, 075136 (2013).
- [35] D. K. Singh and P. Majumdar, *Phys. Rev. B* **96**, 235111 (2017).
- [36] K. Kuroki, S. Onari, R. Arita, H. Usui, Y. Tanaka, H. Kontani and H. Aoki, *Phys. Rev. Lett.* **101**, 087004 (2008).
- [37] D. K. Singh, A. Akbari, and P. Majumdar, *Phys. Rev. B* **98**, 180506(R) (2018).